Rayleigh–Taylor eigenmodes of a thin layer in the nonlinear regime

Mikhail M. Basko[a)]

*Joint Institute for Laboratory Astrophysics, National Institute of Standards and Technology
and University of Colorado, Boulder, Colorado 80309-0440*

In the long-wavelength limit, many aspects of the Rayleigh–Taylor (RT) instability of accelerated fluid shells can be explored by using the thin sheet approximation. For two-dimensional (2-D) planar eigenmodes, analytic nonlinear solutions [E. Ott, Phys. Rev. Lett. **29**, 1429 (1972)] are available. Comparing the simplest of them for the nonconstant acceleration, $g \propto t^{-2}$, with Ott's solution for constant g, the applicability of nonlinear results obtained for constant g to situations with variable acceleration is analyzed. Nonlinear three-dimensional (3-D) effects are investigated by comparing the numerical solutions for axisymmetric Bessel eigenmodes with Ott's solution for 2-D modes. It is shown that there is a qualitative difference between 2-D and 3-D bubbles in the way they rupture a RT unstable fluid shell: In contrast to the exponential thinning of 2-D bubbles, mass is fully eroded from the top of an axisymmetric 3-D bubble within a finite time of $(1.1–1.2)\gamma^{-1}$ after the onset of the free-fall stage; γ is the RT growth rate.

I. INTRODUCTION

Rayleigh–Taylor (RT) instability of thin shells accelerated by ablation pressure is one of the main obstacles to achieving inertially confined thermonuclear fusion in microscopic amounts of a deuterium–tritium mixture.[1] Much effort, both theoretical and experimental, has been devoted to studying the linear and nonlinear aspects of the RT instability in the context of inertial confinement fusion.[2–14] Analysis of the nonlinear stage has practically always relied on sophisticated and costly two-dimensional (2-D)[3–5,7,11] and three-dimensional (3-D) (Ref. 14) hydrodynamic simulations.

To gain a deeper insight into various aspects of the RT instability, analytic and approximate solutions are obviously of special importance. Concerning the instability of accelerated shells, most of the analytic work has focused on calculating linear growth rates in the short-wavelength limit, where the wavelengths of perturbations are small compared to the shell thickness, and the unstable interface can be treated as a boundary between two semi-infinite fluids.[2,9,10,12] The only analytic nonlinear results appear to be those of Layzer,[15] who calculated the vertex speed for axisymmetric and planar bubbles of light fluid rising into heavy fluid.

Numerical simulations in two dimensions[5] indicate that it is unstable modes with relatively long wavelengths $\lambda = (2–8)h$ that are most disruptive for an accelerated shell of unperturbed thickness h. This means that the long-wavelength limit, where a fluid layer can be approximated as an infinitely thin sheet, deserves close scrutiny as well. The more so because equations of motion for a thin sheet are much simpler than the standard (even incompressible) fluid equations and admit a remarkable analytic solution for 2-D planar modes found by Ott,[16] which extends continuously from the linear phase into the deeply nonlinear regime. Having compared the Ott's solution with 2-D incompressible fluid simulations, Manheimer et al.[17] concluded that, being valid in the limit $\lambda \gg h$, the thin sheet approximation is actually quite adequate for wavelengths as small as $\lambda = 2\pi h$. The fruitfulness of this approximation was also convincingly demonstrated by Vishniac,[18] who used it to discover the overstability of the Sedov–Taylor blast waves for small values of the adiabatic index $\gamma_{ad} < 1.2$.

Manheimer et al.[17] were the first to employ the thin sheet approximation to study the 3-D effects in the RT instability of fluid layers. To get rid of unphysically high wave numbers, they performed Fourier transformation of the equations of motion, solved them numerically within a limited domain of k space, and then made the inverse transformation to configuration space. At the same time, it is known that much can be learned about the 3-D behavior by simply examining the axisymmetric (Bessel) eigenmodes in the nonlinear regime and comparing them with the 2-D planar eigenmodes, as was done by Layzer[15] for the axisymmetric and planar bubbles rising into a semi-infinite layer of heavy fluid. Apparently, in what concerns the effects of shape on the nonlinear behavior of 3-D bubbles (or spikes), any 3-D bubble (spike) of general form should exhibit intermediate properties between the 2-D planar and 2-D axial bubbles (spikes), as was actually confirmed by straightforward 3-D simulations in Ref. 14. Nevertheless, no analysis of the nonlinear Bessel modes for thin fluid sheets has been published so far, and the main objective of the present work is to fill this gap.

In Sec. II, the analytic Ott's solution for 2-D planar eigenmodes is briefly revisited and a few dimensionless quantities are introduced, which are later used to characterize the nonlinear behavior of the unstable modes under consideration. Making use of Ott's and another analytic solution from the same family, in Sec. II C we examine how the results obtained for constant acceleration and expressed in terms of the number of *e*-foldings apply to sit-

[a)]1992–93 JILA Visiting Fellow. Permanent address: Institute for Theoretical and Experimental Physics, B. Cheremushkinskaya 25, 117259 Moscow, Russia.

uations with variable acceleration. The nonlinear results for axisymmetric Bessel modes are reported in Sec. III. Since only the central bubble (or the central spike) of Bessel eigenmodes exhibit the 3-D properties of interest here, our analysis is focused on the immediate vicinity of the axis. Accurate numerical results are obtained by expanding the main dynamic variables in powers of the initial radial distance from the axis and reducing the equations of motion to a system of coupled ordinary differential equations for the time dependence of the expansion coefficients. It is shown that, in contrast to the exponential thinning of 2-D bubbles, 3-D bubbles are ruptured explosively, within approximately one growth time after the onset of the free-fall phase. The most conspicuous 3-D effects discussed by Manheimer et al.[17] are clearly manifested by Bessel bubbles as well.

II. 2-D PLANAR MODES

A. Equations of motion and the Ott's solution

Consider a thin horizontal layer of fluid (initially in the xy plane) pushed upward (along z axis) by another massless fluid of pressure P from below. In the thin sheet approximation, the fluid layer is assumed to be infinitely thin but have a finite surface density $\sigma = \sigma(x,y)$. The dynamics of such a fluid sheet is governed by the equations of mass and momentum balance. For motions that occur in the xz plane and do not depend on y (2-D planar modes), these equations are[16]

$$\ddot{x}(t,\xi) = -\frac{P}{\sigma_0} z', \tag{1a}$$

$$\ddot{z}(t,\xi) = \frac{P}{\sigma_0} x', \tag{1b}$$

$$\sigma(t,\xi) = \frac{\sigma_0}{[(x')^2 + (z')^2]^{1/2}}. \tag{2}$$

Here ξ is the Lagrangian coordinate defined such that it coincides with x in the unperturbed state of the fluid sheet, and σ_0 is the unperturbed surface density; the dot and the prime stand for partial derivatives with respect to t and ξ, respectively.

As was first noticed by Ott,[16] Eqs. (1) are linear in x and z, and, for a constant pressure P, their unstable eigenmodes for a given wave number k are

$$x = \xi + a_0 e^{\gamma t} \sin k\xi, \tag{3a}$$

$$z = \tfrac{1}{2} g t^2 + a_0 e^{\gamma t} \cos k\xi. \tag{3b}$$

A remarkable fact is that Eq. (3) describes the evolution of unstable modes all the way from the early linear stage, when $a_0 k e^{\gamma t} \ll 1$, to the advanced nonlinear regime with $a_0 k e^{\gamma t} \gg 1$. Here a_0 is the amplitude of the initial perturbation, and

$$\gamma = (gk)^{1/2} = \left(\frac{P}{\sigma_0} k\right)^{1/2} \tag{4}$$

is the growth rate of the RT instability.

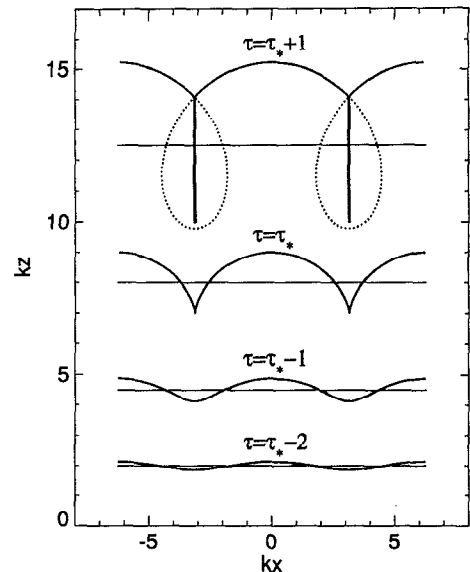Figure 1 shows how the shape of the fluid layer evolves

FIG. 1. Unstable 2-D planar eigenmode of an accelerated thin sheet as given by Ott's solution (3); τ is dimensionless time measured in units of the inverse growth rate γ^{-1}. Evolution of the sheet profile only depends on the time difference $\tau - \tau_*$, where $\tau_* \equiv -\ln(a_0 k)$ is determined by the initial perturbation amplitude a_0. Dotted loops show the unphysical part of the solution: matter from these loops is swept up into vertical spikes (planar ridges), which move by inertia in the laboratory frame.

with dimensionless time

$$\tau \equiv \int_0^t \gamma(t') dt' = \gamma t \tag{5}$$

according to the solution (3). At late enough times, certain segments of this solution (shown as dotted loops on curve $\tau = \tau_* + 1$) become unphysical because Eqs. (1) and (2) do not provide for a possibility of collision between adjacent sheet sections.[16] In reality, matter from unphysical loops forms spikes that move by inertia in the laboratory frame, and fall freely in the accelerated frame associated with the unperturbed sheet motion. A self-consistent way to calculate the fluid motion in spikes, adopted throughout this work, is to assume a perfectly inelastic collision, i.e., to apply the laws of mass and momentum balance to colliding sheet elements at self-intersection points and to ignore the action of pressure forces on the merged segments afterwards. In Fig. 1, thus calculated spikes are shown as vertical walls inside unphysical loops.

B. Main features of planar modes in the nonlinear regime

In the thin sheet approximation—and especially when analytic solutions are available—one can calculate exactly certain quantities that are generally quite useful for characterizing the nonlinear stage of the RT instability of fluid shells, but are difficult to define and evaluate in complex realistic situations. Here, we introduce a few such quantities for Ott's solution with the aim to use them later as the means of comparison between various unstable eigenmodes.
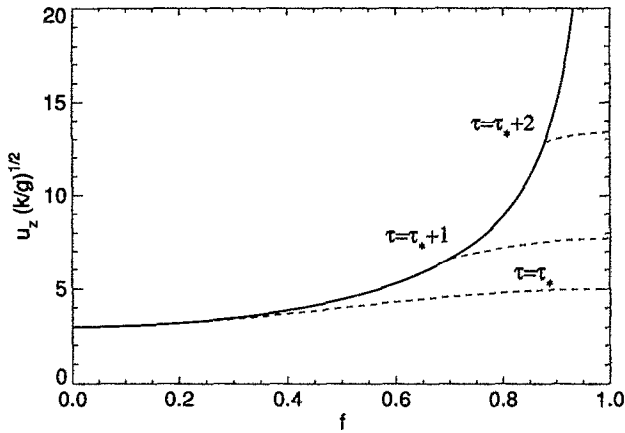
FIG. 2. Distribution of the vertical component of fluid velocity u_z (as measured in the laboratory frame) vs sheet mass fraction f for the 2-D planar eigenmodes (3). Mass fraction f is defined such that $f=0$ and $f=1$ are, respectively, the spike and the bubble centers. Solid curve: the final velocity profile for matter swept up into spikes in the limit $\tau=\gamma t \to \infty$. Dashed curves: velocity distributions at three selected times τ.

A distinctive time moment for solution (3) is

$$\tau_c \equiv \gamma t_c = \tau_* \equiv \ln \frac{1}{|a_0|k}, \tag{6}$$

when cusps appear along the sheet surface (see Fig. 1) at $k\xi_c = \pm\pi, \pm 3\pi,...$ This moment identifies the onset of the free-fall stage for spikes of heavy fluid in the accelerated frame. In the laboratory frame, τ_c marks the termination of acceleration for the bulk of the initial sheet mass. Note that a clearly defined onset time for the free-fall stage is one of the unique features of the thin sheet approximation.

As already mentioned, the sheet material swept up into spikes moves by inertia and preserves its velocity distribution in the laboratory frame. Figure 2 shows the velocity profile of Ott's solution (3) as a function of the sheet mass fraction f defined such that $f=0$ corresponds to the spike tip, and $f=1$ to the bubble top. It is seen that the bulk of the initial sheet mass has a limiting velocity close to the velocity u_{zc} of the spike tip. The latter can be expressed in terms of τ_{uc}—the equivalent time (in units of γ^{-1}) of unperturbed acceleration required to reach the velocity u_{zc}. From Eq. (3b) we have

$$u_{zc} \equiv \dot{z}(t_c, \xi_c) = \tau_{uc} \left(\frac{g}{k}\right)^{1/2} = (\tau_c - 1)\left(\frac{g}{k}\right)^{1/2}, \tag{7}$$

which yields

$$\tau_{uc} = \tau_c - 1. \tag{8}$$

The value of τ_{uc} is useful to know when accelerated motion of fluid shells is simulated with one-dimensional hydrodynamic codes (which cannot reproduce the development of instabilities): τ_{uc} then represents the number of e foldings after which the integration of one-dimensional hydrodynamic equations must be stopped in order to obtain a realistic value of the final velocity of an accelerated unstable shell.

The surface density at the top of rising bubbles decays exponentially

$$\sigma_b(\tau) \equiv \sigma(\tau, 0) = \frac{\sigma_0}{1 + \exp(\tau - \tau_*)}. \tag{9}$$

In other words, 2-D planar bubbles shown in Fig. 1 rupture the shell only in the limit $\tau \to \infty$.

C. Time-dependent acceleration

In practice, the results obtained for a constant acceleration g and expressed in terms of the number of e-foldings τ are often applied to more complex situations where g varies with time. The thin sheet approximation provides an opportunity to check the accuracy of such extrapolation by comparing Ott's solution (3) with another analytic solution of the same type which describes the case of $g \propto t^{-2}$.

Evidently, Eq. (1) admits single-mode solutions analogous to that given by Eq. (3) for any temporal dependence of $g(t) \equiv \sigma_0^{-1} P(t)$. The simplest nontrivial of them is obtained for

$$g(t) = g_0 \left(\frac{t_0}{t}\right)^2. \tag{10}$$

It can be written as

$$x = \xi + a_0 \left(\frac{t}{t_0}\right)^\nu \sin k\xi, \tag{11a}$$

$$z = z_0(t) + a_0 \left(\frac{t}{t_0}\right)^\nu \cos k\xi, \tag{11b}$$

where the exponent $\nu > 1$ is defined by

$$\nu(\nu - 1) = g_0 t_0^2 k \tag{12}$$

and

$$z_0(t) = g_0 t_0^2 \left(\frac{t}{t_0} - 1 - \ln \frac{t}{t_0}\right) \tag{13}$$

is the sheet position in the case of unperturbed motion. In terms of the number of e-foldings

$$\tau \equiv \int_{t_0}^t (gk)^{1/2} dt' = [\nu(\nu-1)]^{1/2} \ln \frac{t}{t_0}, \tag{14}$$

the eigenmode (11) can be rewritten as

$$x = \xi + a_0 \exp\left[\tau \left(\frac{\nu}{\nu-1}\right)^{1/2}\right] \sin k\xi, \tag{15a}$$

$$z = z_0(t) + a_0 \exp\left[\tau \left(\frac{\nu}{\nu-1}\right)^{1/2}\right] \cos k\xi. \tag{15b}$$

Now, the cusps on the sheet profile appear at

$$\tau_c = \left(\frac{\nu-1}{\nu}\right)^{1/2} \tau_*, \tag{16}$$

where τ_* is defined in Eq. (6). The equivalent time of unperturbed acceleration is given by

Mikhail M. Basko

$$\tau_{uc} = \tau_c - [\nu(\nu-1)]^{1/2} \ln \frac{\nu}{\nu-1} ; \qquad (17)$$

the surface density at the bubble top decays as

$$\sigma_b(\tau) = \frac{\sigma_0}{1 + \exp\{\tau[\nu/(\nu-1)]^{1/2} - \tau_*\}} . \qquad (18)$$

Comparing Eqs. (15)–(18) with Eqs. (3), (6), (8), and (9), we conclude that the results obtained for constant g can be applied to the case of $g \propto t^{-2}$ whenever $\nu \gg 1$. Noting that

$$[\nu(\nu-1)]^{1/2} = 2(gk)^{1/2} \left| \frac{g}{\dot{g}} \right| , \qquad (19)$$

we can cast the condition $\nu \gg 1$ in a physically transparent form

$$\left| \frac{\dot{g}}{g} \right| (gk)^{-1/2} \ll 1. \qquad (20)$$

Inequality (20) stipulates that the fractional variation of the acceleration in one growth time should be small compared to unity. In practice, it is sufficient to have $|\dot{g}/g| (gk)^{-1/2} < 0.4$ for Eqs. (16) and (6) to agree within 10%. The last term on the right-hand side of Eq. (17) is very close to unity for all $\nu > 2$, which means that Eq. (8) is an excellent approximation even when $|\dot{g}/g|(gk)^{-1/2} \approx 1$.

III. AXISYMMETRIC BESSEL MODES

With the purpose to look into 3-D effects of the RT instability of a thin layer, we consider only the central bubble and the central spike of the axisymmetric Bessel modes. Strictly speaking, such bubbles and spikes are 2-D objects. Nevertheless, they will be often referred to as 3-D axial bubbles (spikes) because, among possible 3-D shapes, they in many respects represent an opposite extreme to the 2-D planar bubbles (spikes).

A. Equations of motion and methods of solution

Let r be the polar radius in the xy plane. Then, the equations governing the motions of a thin sheet symmetric with respect to the Oz axis are as follows:

$$\ddot{r}(t,\xi) = -\frac{P}{\sigma_0} \frac{r}{\xi} z', \qquad (21a)$$

$$\ddot{z}(t,\xi) = \frac{P}{\sigma_0} \frac{r}{\xi} r', \qquad (21b)$$

$$\sigma(t,\xi) = \frac{r}{\xi} \frac{\sigma_0}{[(r')^2 + (z')^2]^{1/2}} . \qquad (22)$$

Here ξ is the Lagrangian coordinate which coincides with r in the unperturbed state of the fluid sheet. Equations (21a) and (21b) are nonlinear in r and z, and their unstable eigenmodes cannot be obtained analytically even for constant $g = \sigma_0^{-1} P$.

To explore axial eigenmodes in the nonlinear regime, we start with the linear eigenmodes
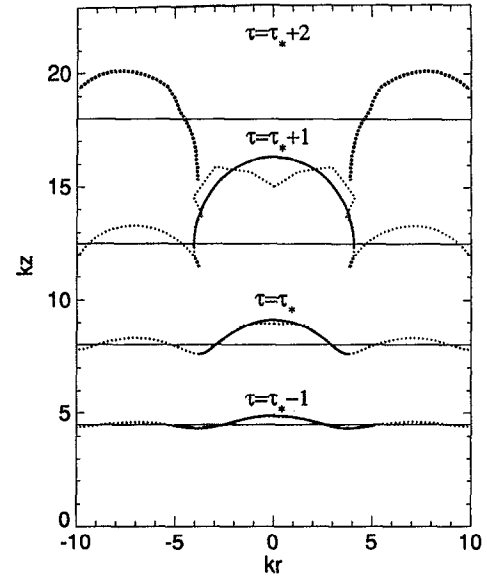

FIG. 3. Temporal evolution of the unstable Bessel eigenmode with bubble in the center. Thick solid curves: power-series solution of Eq. (21). Dotted curves: finite difference solution of Eq. (21). Thick dots show the spikes formed by colliding walls of deepening troughs on the sheet surface. Thin solid lines indicate the positions of the nonperturbed sheet. The initial amplitude a_0 is chosen such that $\tau_* \equiv -\ln(a_0 k) = 4$.

$$r = \xi + a_0 e^{\gamma t} J_1(k\xi), \qquad (23a)$$

$$z = \tfrac{1}{2} g t^2 + a_0 e^{\gamma t} J_0(k\xi). \qquad (23b)$$

Equation (23) provides a solution to Eq. (21) for a given wave number k in the limit $a_0 e^{\gamma t} \ll 1$. Here $J_0(\zeta)$ and $J_1(\zeta)$ are the Bessel functions of the first kind, and γ is given by Eq. (4). Below, having assumed a certain small value of a_0, Eq. (23) (at $t=0$) is used as the initial condition for nonlinear eigenmodes of Eq. (21).

We solve Eqs. (21a) and (21b) numerically, by applying two different techniques described, respectively, in Appendices A and B. The first method is based on the expansion of Eq. (21) in powers of ξ. It yields virtually exact results in the vicinity of the Oz axis, within the convergence radius of the ξ series. The second method employs a straightforward finite difference scheme for Eq. (21); it produces acceptable results at a certain distance from the axis for not too small $|a_0|$ and not too large $\tau \equiv \gamma t$. The two methods are to a certain degree complementary to one another and, when combined, provide adequate solutions for nonlinear Bessel eigenmodes.

B. Results for the central bubble

Nonlinear evolution of the Bessel mode with bubble in the center is shown in Fig. 3. The initial amplitude $a_0 > 0$ is chosen such that $\tau_* = 4$, where τ_* is defined in Eq. (6). The central segment of the sheet profile, shown as a thick solid curve, has been calculated with high precision by the power-series method. However, the convergence radius of this method does not include the tip of the spike ring, as is clearly seen on the $\tau = \tau_* + 1$ curve. The spike parameters cited below have been obtained from the finite difference
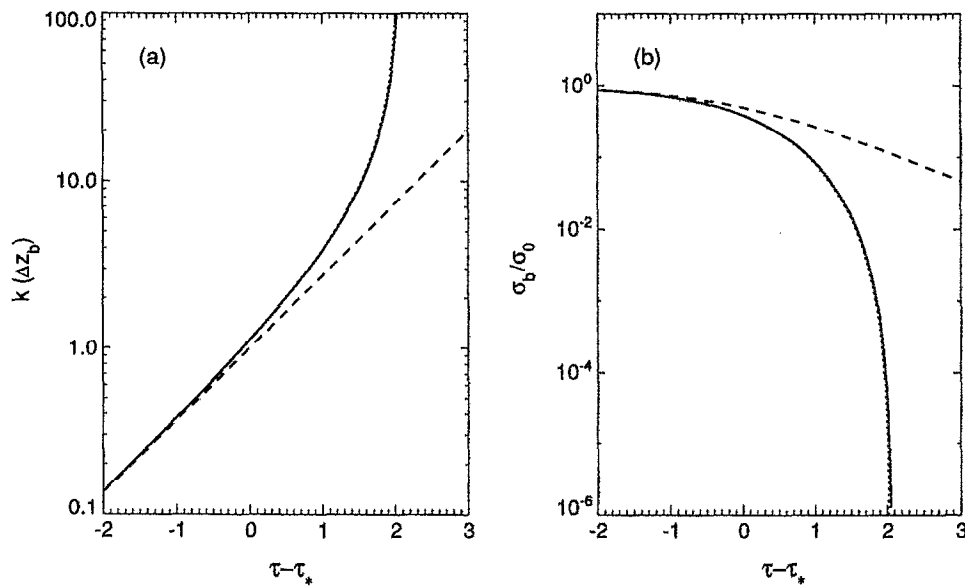
Mikhail M. Basko   1273

FIG. 4. Dynamics of bubble rupture in two (dashes) and three (solid and dots) dimensions. (a) Bubble amplitude in units k^{-1} as a function of dimensionless time $\tau = \gamma t$. (b) Minimum surface density (in units σ_0) as a function of time. Solid and dotted curves correspond, respectively, to $\tau_* = 4$ and 7.

solution, which is plotted with dotted curves. The accuracy of the latter becomes very poor near the axis at $\tau \gtrsim \tau_*$, but remains quite satisfactory in the vicinity of the spike ring around the time of its formation so long as $\tau_* \lesssim 4$–5. If we try to increase τ_* by decreasing the initial amplitude a_0, we still obtain good power-series results, while the finite difference solution tends to be increasingly dominated by short-wavelength ripples and becomes virtually worthless.

A fundamental qualitative difference between the 3-D bubble in Fig. 3 and the 2-D bubble in Fig. 1 is that the 3-D bubble is ruptured not exponentially, in the limit $\tau \to \infty$, but explosively, within a finite interval of time. By the time $\tau = \tau_* + 2$, the surface of the central bubble in Fig. 3 has been blown out far beyond the rz range of the plot, and the remaining segments plotted with thick dots show the spike material that moves by inertia.

The process of explosive 3-D bubble rupture is clearly illustrated in Fig. 4. It is seen that, as dimensionless time τ approaches the rupture moment τ_r, the bubble amplitude

$$\Delta z_b = z(t,0) - \tfrac{1}{2} g t^2$$

tends to infinity [Fig. 4(a)], while the minimum surface density $\sigma_b = \sigma(t,0)$ at the top of the bubble goes to zero [Fig. 4(b)]. For comparison, dashed lines in Figs. 4(a) and 4(b) show the temporal behavior of the corresponding quantities for the 2-D solution (3). Because a linear eigenmode (23) is used as the initial condition for the nonlinear regime, the values of $\tau_r - \tau_*$ that we calculate depend weakly on τ_*. Evidently, the difference $\tau_r - \tau_*$ should approach certain constant as $\tau_* \to \infty$. Our calculations with the power-series method yield

$$\tau_r - \tau_* = \begin{cases} 2.07, & \tau_* = 4, \\ 2.05, & \tau_* = 7. \end{cases} \qquad (24)$$

The difference in the way the 2-D and 3-D bubbles are ruptured can be easily explained by means of the following scaling argument. Let $R = R(t)$ be a characteristic scale for the bubble radius. Then, the equation of motion for an element of the bubble surface can be written as

$$\sigma \ddot{R} = P, \qquad (25)$$

where the surface density $\sigma(t)$ scales as

$$\sigma = \begin{cases} \dfrac{\sigma_0}{kR}, & \text{2-D bubble,} \\[2mm] \dfrac{\sigma_0}{(kR)^2}, & \text{3-D bubble.} \end{cases} \qquad (26)$$

Substituting Eq. (26) into Eq. (25), we obtain 2-D and 3-D differential equations for $R(t)$

$$\ddot{R} = \begin{cases} \gamma^2 R, & \text{2-D bubble,} \\ \gamma^2 k R^2, & \text{3-D bubble,} \end{cases} \qquad (27)$$

which yield the following asymptotic laws of bubble rupture:

$$\frac{\sigma}{\sigma_0} \propto \begin{cases} e^{-\tau}, & \text{2-D bubble,} \qquad (28a) \\[2mm] \left(1 - \dfrac{\tau}{\tau_r}\right)^2, & \text{3-D bubble.} \qquad (28b) \end{cases}$$

Obviously, the difference between these two asymptotic expressions is due to the additional geometrical factor R^{-1} in the scaling of σ with R for the 3-D bubbles. To verify how adequately the simple Eq. (28b) reproduces the erosion of mass from the top of the Bessel bubble, in Fig. 5 we have plotted the square root of the ratio σ_b/σ_0 versus $\tau - \tau_*$, as calculated with the power-series method. Since both curves, obtained, respectively, for $\tau_* = 4$ and 7, are almost straight lines, we conclude that Eq. (28b), if not exact,
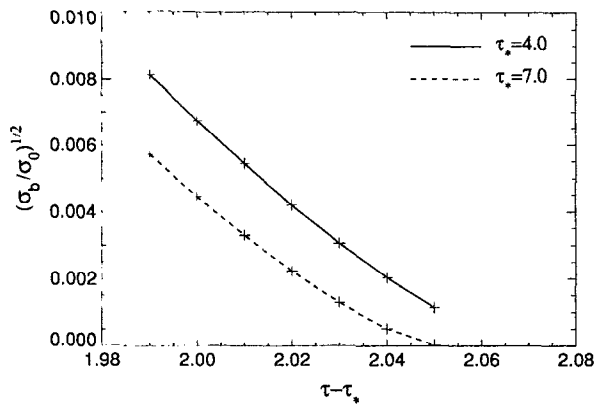
Mikhail M. Basko

FIG. 5. Temporal behavior near the rupture time $\tau = \tau_r$ of the square root of the sheet thickness σ_b calculated for the vertex point of the central Bessel bubble for two values of $\tau_* \equiv -\ln(a_0 k)$. The calculated values of σ_b are shown with crosses; the solid and the dashed curves are drawn to guide the eye.
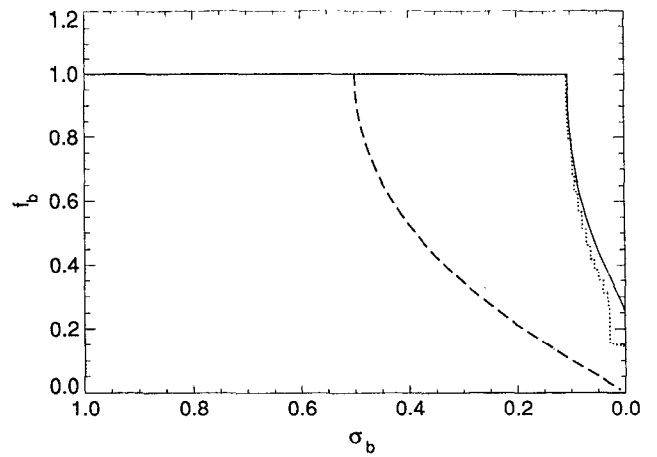

FIG. 6. Fraction of the sheet mass f_b left outside freely falling spikes (fractional bubble mass) as a function of the sheet surface density σ_b at the top of rising bubbles. For the Bessel eigenmode (thin solid and dotted curves), only the central bubble within the first cusp at $\xi < \xi_c = 3.8317 k^{-1}$ is considered. Solid and dotted curves correspond to two different methods of evaluating f_b for the central Bessel bubble. Dashed curve shows the results for the 2-D planar eigenmode (3).

does indeed give a good approximation to the asymptotic behavior of 3-D bubbles near rupture time τ_r.

As is apparent from physical considerations, the first cusp on the Bessel mode appears around the central bubble at

$$k\xi_c = j_{1,1} = 3.8317,$$

with a zero radial component of the fluid velocity, $u_{rc} \equiv \dot{r}(t_c, \xi_c) = 0$; here $j_{1,1}$ is the first zero of the Bessel function $J_1(\zeta)$. Other cusp parameters evaluated from the finite difference solution for $\tau_* = 4$ are as follows:

$$\tau_c = \tau_* + 0.91, \tag{29a}$$

$$k(\Delta z_c) = -1.0, \tag{29b}$$

$$\tau_{uc} = u_{zc}\left(\frac{k}{g}\right)^{1/2} = \tau_* - 0.09. \tag{29c}$$

Equation (29a) tells us that the spike ridge around the axisymmetric bubble forms approximately one growth time later than the spikes of 2-D planar modes do [cf. Eq. (6)]. Equations (29a) and (29c) imply that Eq. (8) holds for the central Bessel bubble as well. Shell parameters at the bubble top ($\xi = 0$) at the time of cusp formation $\tau = \tau_c$ are

$$k(\Delta z_b) = 3.39, \tag{30a}$$

$$u_{zb}\left(\frac{k}{g}\right)^{1/2} = \tau_* + 5.61, \tag{30b}$$

$$\frac{\sigma_b}{\sigma_0} = 0.11. \tag{30c}$$

From Eqs. (29b) and (30a) we infer that the full spike-to-bubble amplitude of the shell distortion at the onset of the free-fall stage is $k(z_b - z_c) = 4.4$.

It should be noted here that far from the central axis, evolution of the Bessel modes approaches that of the planar modes described by Eq. (3). This implies that certain nonlinear characteristics of Bessel modes observed at $k\xi \gg 1$ can be obtained by simply extrapolating the linear solution

(23) into the nonlinear regime. For example, the parameters of the first cusp at $k\xi_c = 3.8317$ calculated in this manner coincide (within the accuracy of the finite difference method) with those given by Eq. (29).

Earlier, Manheimer et al.[17] noticed that the nonlinear growth of 2-D and 3-D bubbles looks strikingly different when the fractional bubble mass f_b is plotted versus its minimum surface density σ_b. After we construct a similar plot for the central Bessel bubble (see Fig. 6), we obtain practically the same result, even in a somewhat more conspicuous form. In Fig. 6, the values of σ_b for the Bessel bubble have been precisely calculated with the power expansion technique. The bubble mass fraction f_b was evaluated by using two less accurate methods, namely, (i) from the finite difference solution (dotted curve), and (ii) by extrapolating the linear expressions (23) into the nonlinear regime (Bessel approximation; thin solid curve). The difference between the two methods characterizes the accuracy of each of them.

Figure 6 and Eq. (30c) demonstrate that the axisymmetric 3-D bubble begins to lose mass into the neighboring spike only after it thins out to $\sigma_b = 0.11\sigma_0$, as contrasted to $\sigma_b = 0.5\sigma_0$ in the 2-D case. One can expect that in a more general case of nonaxial 3-D bubbles the f_b versus σ_b curves should pass between the two extreme examples plotted in Fig. 6. This agrees very well with simulation results obtained in Ref. 17 by using a considerably more complex numerical method. A manifest difference between the 2-D and 3-D bubbles exhibited by Fig. 6 has, of course, the same explanation as the difference between the 2-D and 3-D rupture asymptotes in Eq. (28).

After the central bubble of the Bessel eigenmode has been ruptured and its material dispersed, the adjacent spike ridge moves by inertia. Figure 7 portrays this motion as calculated with the finite difference method. The momenta of colliding sheet segments that form the spike add up in
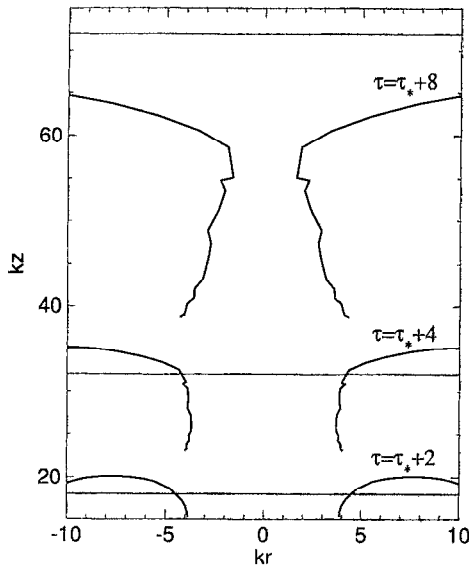
Phys. Plasmas, Vol. 1, No. 5, May 1994

Mikhail M. Basko   1275

FIG. 7. Motion of the sheet material surrounding the central Bessel bubble after the latter has been ruptured at $\tau=\tau_*+2.07$. Rugged appearance of the sheet profile reflects the limited accuracy of the finite difference method.

FIG. 8. Same as Fig. 3 but for the spike in the center of the Bessel eigenmode [$a_0<0$ in Eq. (23)].

such a way that a significant portion of the spike material has negative final values of the radial velocity u_r (recall that the radial velocity of the lower spike tip is $u_{rc}=0$). As a result, the hole left behind the ruptured bubble eventually closes up with converging spike material. A similar effect has been observed in 3-D hydrodynamic simulations by Dahlburg et al.[14]

C. Results for the central spike

If we take a negative value of the initial amplitude a_0 in Eq. (23), such a mode evolves into a needle-like central spike shown in Fig. 8. With regard to their formation dynamics, the 3-D axial and 2-D planar spikes differ only quantitatively. The parameters of the central cusp

$$\tau_c=\tau_*+\begin{cases}1.187, & \tau_*=4, \\ 1.199, & \tau_*=7,\end{cases}\tag{31a}$$

$$k(\Delta z_c)=\begin{cases}-2.463, & \tau_*=4, \\ -2.473, & \tau_*=7,\end{cases}\tag{31b}$$

$$\tau_{uc}=u_{zc}\left(\frac{k}{g}\right)^{1/2}=\tau_*-\begin{cases}0.676, & \tau_*=4, \\ 0.668, & \tau_*=7,\end{cases}\tag{31c}$$

and of the circular bubble around it at the time of cusp formation

$$k(\Delta z_b)=\begin{cases}1.342, & \tau_*=4, \\ 1.362, & \tau_*=7,\end{cases}\tag{32a}$$

$$u_{zb}\left(\frac{k}{g}\right)^{1/2}=\tau_*+\begin{cases}2.563, & \tau_*=4, \\ 2.598, & \tau_*=7,\end{cases}\tag{32b}$$

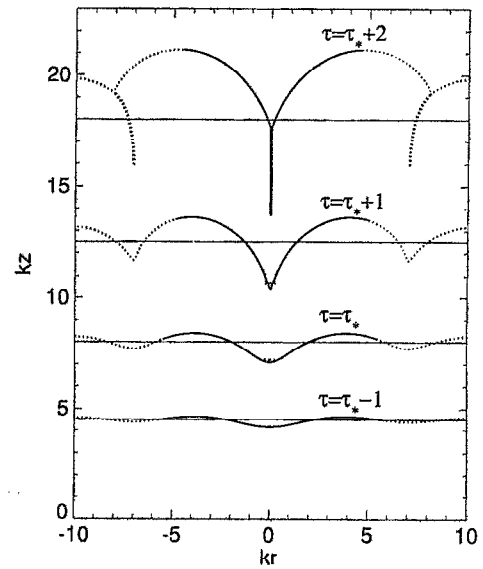$$\frac{\sigma_b}{\sigma_0}=\begin{cases}0.410, & \tau_*=4, \\ 0.405, & \tau_*=7,\end{cases}\tag{32c}$$

can be accurately calculated with the power-series method. Note that although the central spike forms somewhat later than the circular ridge around the central bubble [cf. Eqs. (29a) and (31a)], the final fluid velocity at its tip [Eq. (31c)] is lower than the corresponding value for the circular ridge [Eq. (29c)].

IV. DISCUSSION AND CONCLUSIONS

The thin sheet approximation provides a unique opportunity to explore certain nonlinear effects of the RT instability of accelerated fluid shells with relatively simple mathematical methods. For 2-D planar eigenmodes, simple analytic solutions exist in at least two cases: for a constant acceleration g of an unstable fluid layer[16] and for $g\propto t^{-2}$. By comparing these two solutions, we conclude that the nonlinear results obtained for a constant g and expressed in terms of the number of e-foldings $\tau=\gamma t$ apply to the $g\propto t^{-2}$ case whenever $|\dot{g}/g|(gk)^{-1/2}<0.4$. A similar analysis can be conducted for any dependence $g=g(t)$ by integrating simple ordinary differential equations for the amplitudes of nonlinear 2-D modes.

To get insight into nonlinear 3-D effects, we have considered the axisymmetric Bessel eigenmodes and compared them to the 2-D planar modes. Having solved the equations of motion with high enough accuracy by a power-series method in the vicinity of the central axis, we found that 3-D bubbles rupture a RT unstable fluid shell explosively, within approximately one growth time after the onset of the nonlinear regime. Even though derived in the thin sheet limit, this result should apply quite generally to any fluid layer of finite thickness with an arbitrary spectrum of initial disturbances. Indeed, even when no long-wavelength perturbations are initially present, a shell with unperturbed thickness h is eventually ruptured by bubbles with characteristic wavelengths $\sim h$. As any of such bub-

Mikhail M. Basko

bles rises toward the upper fluid boundary, the fluid layer above the bubble rapidly thins out, and the thin sheet approximation becomes increasingly more accurate in the vicinity of the bubble top. One should keep in mind, however, that the explosive rupture of 3-D bubbles occurs only in the limit of vanishing density of the light fluid, $\rho_l \rightarrow 0$. In reality, the bubble vertex cannot rise significantly faster than the sound speed in the light fluid, $c_{sl} \simeq (P/\rho_l)^{1/2}$.

It is well known that when RT unstable eigenmodes of an interface between two semi-infinite fluids reach the nonlinear regime, they saturate in the sense that the exponential growth of light-fluid bubbles changes to an ascent with a constant speed. Three-dimensional fluid simulations[14] have confirmed that, among various 3-D shapes, the 2-D planar and the axisymmetric Bessel bubbles are, respectively, the first and the last to saturate. Accordingly, the asymptotic rising velocity of the Bessel bubbles, as calculated by Layzer,[15] is $\sqrt{3}$ times higher than that of the 2-D planar bubbles with the same wave number k. In contrast, no saturation in such sense occurs for long-wavelength bubbles that evolve along thin fluid sheets. Instead, the exponential growth of 2-D planar eigenmodes persists all the way into the nonlinear regime.[16] The Bessel bubbles rise even faster: they "explode" to an infinite amplitude within a finite time of $\simeq (gk)^{-1/2}$ after entering the nonlinear stage (see Fig. 4). As a result, we reach the same conclusion for the thin sheet modes as was established for the unstable interface between two half spaces,[14] namely, that the most disruptive are 3-D modes with round-shaped bubbles.

Instead of saturation times, the times τ_c of the onset of the free-fall stage, or the equivalent times of unperturbed acceleration τ_{uc} can be used to order thin sheet modes of different shapes. Our calculations have revealed that (i) the 2-D planar modes first reach the free-fall stage, followed in order by (ii) the central Bessel bubble, and (iii) the central Bessel spike. With respect to progressively increasing values of τ_{uc} (which represent the minima of the final velocity distribution in the laboratory frame), the order is as follows: (i) the 2-D planar modes, (ii) the central Bessel spike, and (iii) the central Bessel bubble. The latter ordering coincides with that found by Dahlburg et al.[14] in their 3-D simulations of the saturation of modes with $kh \sim 1$.

ACKNOWLEDGMENT

APPENDIX A: POWER-SERIES SOLUTION OF EQ. (21)

Introducing dimensionless variables

$$\bar{r}=kr, \quad \bar{z}=kz, \quad \tau=(gk)^{1/2}t, \quad \zeta=k\xi, \quad \bar{a}_0=ka_0 \qquad (A1)$$

we can rewrite Eq. (21) as

$$\ddot{\bar{r}}(\tau,\zeta)=-\frac{\bar{r}}{\zeta}\bar{z}',$$

$$\ddot{\bar{z}}(\tau,\zeta)=\frac{\bar{r}}{\zeta}\bar{r}'. \qquad (A2)$$

We seek a solution to Eq. (A2) which satisfies the initial condition

$$\bar{r}(0,\zeta)=\zeta+\bar{a}_0 J_1(\zeta),$$

$$\bar{z}(0,\zeta)=\bar{a}_0 J_0(\zeta). \qquad (A3)$$

It is easy to verify that the general expansion of such a solution into powers of ζ can be cast in the form

$$\bar{r}(\tau,\zeta)=\zeta+\tfrac{1}{2}\bar{a}_0\zeta[b_1-b_2\zeta^2+b_3\zeta^4-\cdots+(-1)^{i-1}b_i\zeta^{2i-2}$$
$$+\cdots], \qquad (A4)$$

$$\bar{z}(\tau,\zeta)=\tfrac{1}{2}\tau^2+\bar{a}_0[a_1-a_2\zeta^2+a_3\zeta^4-\cdots+(-1)^{i-1}a_i\zeta^{2i-2}$$
$$+\cdots],$$

where the expansion coefficients $a_i=a_i(\tau)$, $b_i=b_i(\tau)$, $i=1,2,3,\ldots$, are functions of time. Substituting Eq. (A4) into Eq. (A2), we obtain the following infinite set of coupled ordinary differential equations (ODE) for a_i, b_i:

$$\ddot{a}_i(\tau)=i\left(b_i+\frac{\bar{a}_0}{4}\sum_{j=1}^{i}b_j b_{i-j+1}\right),$$

$$\ddot{b}_i(\tau)=4ia_{i+1}+2\bar{a}_0\sum_{j=1}^{i}ja_{j+1}b_{i-j+1}. \qquad (A5)$$

The initial values

$$a_i(0)=\frac{1}{4^{i-1}[(i-1)!]^2}, \quad b_i(0)=\frac{a_i(0)}{i} \qquad (A6)$$

are determined by the expansion of Bessel functions in Eq. (A3) into powers of ζ. In numerical calculations, the infinite series of ODE (A5) were truncated at a certain $i=n$ by imposing a condition

$$a_{n+1}=\frac{a_n}{4n^2}, \qquad (A7)$$

which holds exactly for the linear solution (23). In addition, because of the limited range of real numbers available on computers, a rescaling procedure was adopted for the values of a_i, b_i; most of the runs were performed with $n=20$–40.

APPENDIX B: FINITE DIFFERENCE SCHEME FOR EQ. (21)

Replacing ζ with a mass coordinate

$$m=\tfrac{1}{2}\zeta^2 \qquad (B1)$$

we can rewrite Eq. (A2) as

$$\frac{\partial \bar{r}}{\partial \tau}=\bar{u}_r, \quad \frac{\partial \bar{u}_r}{\partial \tau}=-\bar{r}\frac{\partial \bar{z}}{\partial m},$$

$$\frac{\partial \bar{z}}{\partial \tau}=\bar{u}_z, \quad \frac{\partial \bar{u}_z}{\partial \tau}=\frac{1}{2}\frac{\partial \bar{r}^2}{\partial m}. \qquad (B2)$$

Equation (B2) has been discretized on a grid m_i,τ_j to the second order in space and time

$$\bar{r}_i^{j+1/2}=\bar{r}_i^j+\tfrac{1}{2}(\tau_{j+1}-\tau_j)(\bar{u}_r)_i^j,$$

$$\bar{z}_i^{j+1/2}=\bar{z}_i^j+\tfrac{1}{2}(\tau_{j+1}-\tau_j)(\bar{u}_z)_i^j,$$

(B3)

$$(\bar{u}_r)_i^{j+1}=(\bar{u}_r)_i^j-\bar{r}_i^{j+1/2}\left(\frac{\partial \bar{z}}{\partial m}\right)_i^{j+1/2},$$

$$(\bar{u}_z)_i^{j+1}=(\bar{u}_z)_i^j+\frac{1}{2}\left(\frac{\partial \bar{r}^2}{\partial m}\right)_i^{j+1/2},$$

(B4)

$$\bar{r}_i^{j+1}=\bar{r}_i^{j+1/2}+\tfrac{1}{2}(\tau_{j+1}-\tau_j)(\bar{u}_r)_i^{j+1},$$

$$\bar{z}_i^{j+1}=\bar{z}_i^{j+1/2}+\tfrac{1}{2}(\tau_{j+1}-\tau_j)(\bar{u}_z)_i^{j+1}.$$

(B5)

Partial derivatives with respect to m on the right-hand side of Eq. (B4) are evaluated as

$$\left(\frac{\partial X}{\partial m}\right)_i^{j+1/2}=\frac{m_{i+1}-m_i}{m_i-m_{i-1}}\frac{X_i^{j+1/2}-X_{i-1}^{j+1/2}}{m_{i+1}-m_{i-1}}$$

$$+\frac{m_i-m_{i-1}}{m_{i+1}-m_i}\frac{X_{i+1}^{j+1/2}-X_i^{j+1/2}}{m_{i+1}-m_{i-1}},$$

(B6)

where X is any of the two quantities $\bar{z}$ or $\bar{r}^2$.

[1] J. D. Lindl, R. L. McCrory, and E. M. Campbell, Phys. Today 45 (9), 32 (1992).
[2] S. E. Bodner, Phys. Rev. Lett. 33, 761 (1974).
[3] J. D. Lindl and W. C. Mead, Phys. Rev. Lett. 34, 1273 (1975).
[4] C. P. Verdon, R. L. McCrory, R. L. Morse, G. R. Baker, D. I. Meiron, and S. A. Orszag, Phys. Fluids 25, 1653 (1982).
[5] M. H. Emery, J. H. Gardner, and J. P. Boris, Appl. Phys. Lett. 41, 808 (1982); 48, 1406 (1989).
[6] H. Takabe, L. Montierth, and R. L. Morse, Phys. Fluids 26, 2299 (1983); H. Takabe, K. Mima, L. Montierth, and R. L. Morse, ibid. 28, 3676 (1985).
[7] D. L. Youngs, Physica D 12, 32 (1984).
[8] K. I. Read, Physica D 12, 45 (1984).
[9] H. J. Kull and S. I. Anisimov, Phys. Fluids 29, 2067 (1986).
[10] H. J. Kull, Phys. Fluids B 1, 170 (1989).
[11] M. Tabak, D. H. Munro, and J. D. Lindl, Phys. Fluids B 2, 1007 (1990).
[12] A. B. Bud'ko and M. A. Liberman, Phys. Fluids B 4, 3499 (1992).
[13] B. A. Remington, S. V. Weber, S. W. Haan, J. D. Kilkenny, S. G. Glendinning, R. J. Wallace, W. H. Goldstein, B. G. Wilson, and J. K. Nash, Phys. Fluids B 5, 2589 (1993).
[14] J. P. Dahlburg, J. H. Gardner, G. D. Doolen, and S. W. Haan, Phys. Fluids B 5, 571 (1993).
[15] D. Layzer, Astrophys. J. 122, 1 (1955).
[16] E. Ott, Phys. Rev. Lett. 29, 1429 (1972).
[17] W. Manheimer, D. Colombant, and E. Ott, Phys. Fluids 27, 2164 (1984).
[18] E. T. Vishniac, Astrophys. J. 274, 152 (1983).

Mikhail M. Basko